Soft Matter

Primitive chain network simulations for the interrupted shear response of entangled polymeric liquids

Journal:	*Soft Matter*
Manuscript ID	SM-ART-04-2020-000654.R1
Article Type:	Paper
Date Submitted by the Author:	12-Jun-2020
Complete List of Authors:	Masubuchi, Yuichi; Nagoya University, Department of Materials Physics Doi, Yuya; Nagoya University, Department of Materials Physics Uneyama, Takashi; Nagoya University, Department of Materials Physics

Primitive chain network simulations for the interrupted shear response of entangled polymeric liquids

Yuichi Masubuchi[1,2*], Yuya Doi[2] and Takashi Uneyama[1,2]
[1]Center of Computational Science, and [2]Department of Materials Physics, Nagoya University, Nagoya 4648603, Japan.

*To whom correspondence should be addressed
mas@mp.pse.nagoya-u.ac.jp

ABSTRACT

The non-linear viscoelastic response under interrupted shear flows is one of the interesting characteristics of entangled polymers. In particular, the stress overshoot in the resumed shear has been discussed concerning the recovery of the entanglement network in some studies. In this study, we performed multi-chain slip-link simulations to observe the molecular structure of an entangled polymer melt. After confirming the reasonable reproducibility of our simulation with the literature data, we analyzed the molecular characteristics following the decoupling approximation. We reasonably found that the segment orientation dominates the stress overshoot even under the resumed shear with minor contributions from the segment stretch and entanglement density. We defined the mitigation function for the recovery of stress overshoot as a function of the rest time and compared it with the relaxation of the molecular quantities after the initial shear. As a result, we have found that the mitigation of stress overshoot coincides with the relaxation of entanglement density.

Keywords

viscoelasticity, polymers, molecular simulation

INTRODUCTION

Stress growth under interrupted shear flows is one of the interesting non-linear viscoelastic behaviors of entangled polymers[1,2]. In this rheological test, an equilibrated polymeric liquid is subjected to fast, steady shear. After a certain amount of applied shear, the flow is interrupted to relax the material. During the relaxation, before reaching equilibrium, the material is exposed to the second shear. The material response under the second shear depends on the interval between initial and resumed flows-the so-called rest time. With a sufficiently long rest time, the material equilibrates, and the stress growth under resumed flow is identical to that under the initial flow. More specifically, the stress increases up to a strain of approximately 2 to 3 and shows an overshoot

before reaching a steady value. The maximum stress at the overshoot monotonically decreases with decreasing rest time. Because no overshoot occurs in the absence of a rest, the decline of the overshoot is intuitive in a qualitative sense. However, no quantitative explanation has been established.

In some studies, the mitigation of stress overshoot has been attributed to a structural change of the entanglement network. To our knowledge, network modification under deformation was firstly mentioned by Tobolsky et al.[3,4] according to the transient network idea. Graessley[5] described the shear thinning of polymeric liquids by considering the rates of creation and destruction of entanglements. Doi and Edwards[6] derived the universal damping function under large step shear deformations from the loss of entanglements induced by chain contraction. Similar discussions have been made for interrupted shear[7–11].

The non-linear response under interrupted shear is not necessarily solely due to modification of the entanglement network. For example, Santangelo and Roland[12] showed that an unentangled polystyrene melt exhibits similar rest time dependence of stress overshoot. They mentioned that the suppression of overshoot is due to the unrelaxed segmental orientation. Even for entangled polymers, orientation contributes to stress, as discussed for the stress overshoot during the initial shear[13–16] on the basis of the stress-optical law. Indeed, Ianniruberto and Marrucci[17] demonstrated that the integral constitutive equation proposed by Doi and Edwards[18] qualitatively reproduces the interrupted shear results reported by Wang et al.[11], even though the model incorporates neither chain stretch nor loss of entanglement. In addition, Graham et al.[19] semi-quantitatively reproduced the data of Wang et al. [11] using a tube model, in which chain stretch is incorporated but the entanglement density is unchanged. Nevertheless, as noted by Ianniruberto and Marrucci[17], further studies are required to discriminate the contributions from orientation, stretch and entanglement density in the stress response under interrupted shear.

In this study, through the multi-chain slip-link simulation (the so-called primitive chain network (PCN) simulation[20–23]), we investigated the stress response of an entangled polymer melt under interrupted shear flows. The observed stress response was in reasonable agreement with the experimental results of Roy and Roland[24]. We obtained the time development of segmental orientation, stretch, and entanglement density separately. The results demonstrate that, for the stress overshoot, the contribution from the orientation is dominant, whereas the contribution from the entanglement density is minor. Meanwhile, the mitigation of overshoot coincides with the relaxation of entanglement density.

MODEL AND SIMULATIONS

Because the model and code used in this study are the same as those used for previous studies[25–29], only a brief description is given here. A melt of entangled polymer was replaced by a network consisting of network nodes, strands and dangling ends. Each polymer chain was represented by a path connecting two dangling ends through the nodes and strands. At each node, a slip-link was positioned to bundle two chains according to the binary assumption of entanglement. The slip-link allows sliding of the bundled chains, and it is destroyed if one of the chains slides off. By contrast, when a chain end protrudes from the connected slip-link by a critical amount, a new slip-link is created on the dangling segment by hooking another strand within a cut-off distance equal to the average strand length at equilibrium. The position of the slip-link obeys a Langevin-type equation of motion, in which the force balance is considered among the drag force, osmotic force, tension acting on diverging strands, and the random force. The chain sliding is described by a rate equation for the number of Kuhn segments on each strand. The transport rate of the Kuhn segments between consecutive strands is calculated along the chain according to the force balance considered for the slip-link position.

As summarized earlier[21–23], the PCN model is located in a niche between the tube[30–32] and the bead-spring[33] models; namely, the unit of calculation is the entanglement segment, which is also used in single-chain slip-link models[34–37]. Meanwhile, the multi-chain dynamics is calculated as performed for the bead-spring simulations and the other coarse-grained models that prohibits chain crossing[33,38–40]. The multi-chain nature of the model excludes the mean-field type assumptions for thermal[41–43] and convective[44] constraint release. The disturbance from the affine deformation owing to the force balance around the entanglement[45] is also considered. The multi-chain construction was followed by multi-chain slip-spring models[46–49], in which many Rouse chains dispersed in a simulation box are connected by virtual springs. Except for the level of coarse-graining, these multi-chain models exhibit similar features to reproduce entangled polymer dynamics[50].

In this study, we examined the experiment reported by Roy and Roland[24] for a polyisobutylene (PIB) melt ($M_w = 46{,}000$ and $M_w/M_n = 3.2$). From this value of M_w, we determined the number of strands per chain was $Z_0 = 12$. This value of Z_0 means that the molecular weight carried by a single network strand is $M_0 = M_w/Z_0 \sim 3800$. We note that M_0 is much smaller than the entanglement molecular weight $M_\mathrm{e} = 9400$[24]. This difference is due to the additional fluctuations implemented in the PCN model[51,52]. We also note that the value of M_0 determines the unit of modulus, G_0, by the dimensional analysis as $G_0 = \rho RT/M_0$, where ρ is the density. Although this relation works well for monodisperse systems, in this specific study, G_0 was determined independently of M_0 to accommodate for the effect of the molecular weight distribution (MWD) in

the experiment[24], as shown later. Nevertheless, for simplicity in the molecular analysis, we simulated the monodisperse system. The simulations were performed with non-dimensional units, where the units of length, energy, and time were chosen as the average strand length, a, thermal energy, $k_{\mathrm{B}}T$, and the diffusion time for a node, $\tau_0 = \zeta a^2/6k_{\mathrm{B}}T$. Here, ζ is the friction of the single node. The simulation box dimension was 16^3, which is sufficiently larger than the chain dimension even under fast shear. The end-to-end distance $\sqrt{\langle \mathbf{R}^2 \rangle}$ was 3.7 at equilibrium, and 8.2 under the fastest shear among all examined shear rates. The strand number density under equilibrium was 10. For this system, the Rouse time is given as $\tau_{\mathrm{R}} = {Z_0}^2/2\pi^2 = 7.3\tau_0$ according to a previous study[53]. The longest relaxation time for the viscoelastic relaxation was obtained from the equilibrium simulation[50,54] as $\tau_d = 77\tau_0$. To resolve the slight changes in stress, we performed 24 independent simulation runs for each condition for different initial equilibrated configurations.

RESULTS AND DISCUSSION

Comparison with the experimental results

Figure 1 shows the linear viscoelasticity of the sample. Comparison between the experimental data (symbols) and the simulation results (curves) gives the model parameters as G_0 = 0.174 MPa, and τ_0 = 0.021 s. As we mentioned in the previous section, G_0 must generally be determined from M_0. However, in this specific study, we optimized G_0 separately from M_0 to accommodate for the effects of the MWD on the compliance (i.e., the crossover between G' and G''). The value of τ_0 was determined to reproduce the longest relaxation mode.

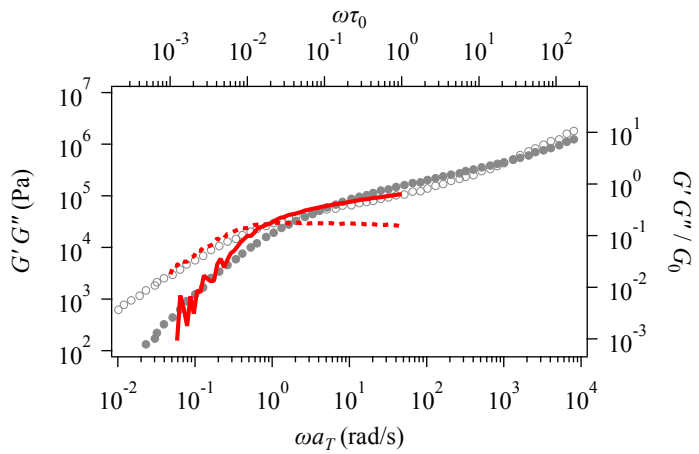

Figure 1 Linear viscoelasticity. The filled and unfilled circles are the experimental data taken from the literature[24]. The solid and broken curves are the simulation results.

Figure 2 shows the viscosity growth under start-up shear from equilibrium. The experimental data[24] are shown for comparison. The simulation reproduces the viscosity overshoot and shear thinning only qualitatively. In particular, the steady state viscosity is overestimated in the simulation. Similar

discrepancies have been reported even for monodisperse systems[25–29]. The tube model also has a similar feature, and the mechanism of this discrepancy is unknown. Nevertheless, hereafter, we discuss the response under 1 sec^{-1} in detail.

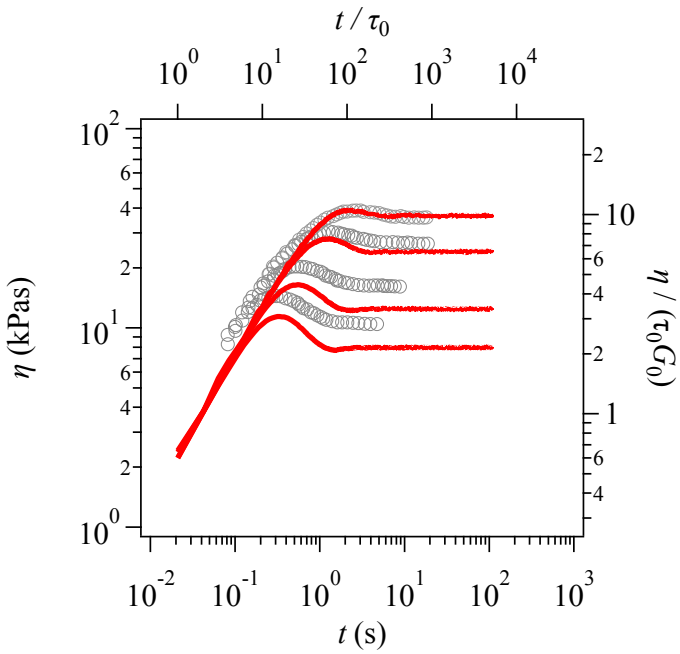

Figure 2 Viscosity growth under start-up shear at shear rates of 1, 2, 5 and 10 sec^{-1} from top to bottom. The solid curves and symbols represent the simulation and experimental results[24], respectively.

Figure 3 shows the viscosity growth under resumed shear at a shear rate of $1s^{-1}$. The prediction for the first start-up run (black curve) exhibits a discrepancy from the experimental data (black symbols) in this comparison. Indeed, the stress fluctuations in the simulation are concealed in the double-log plot in Figure 2, whereas they are visible in Figure 3 even after ensemble averaging for 24 independent simulation runs, as shown by the red thin curve for a rest time of 2 s. To extract the peak, we smoothed the simulation results using the second-order Savitzky-Golay method[55]. For the smoothed curves, the simulation qualitatively captures the experiment; namely, the magnitude of the viscosity overshoot increases with increasing rest time to recover the behavior exhibited under initial shear. Possibly owing to the MWD, the simulated viscosity decreases to a steady value faster than the experimental one.

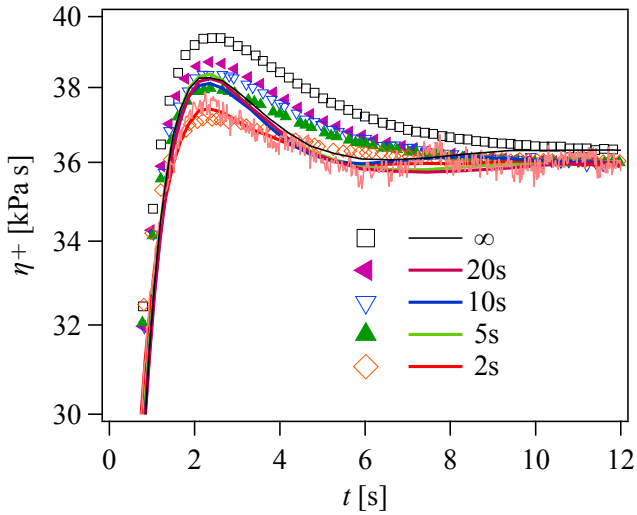

Figure 3 Viscosity growth under resumed shear at a shear rate of 1s^{-1} for various rest times after the initial shear. The data for the initial startup run are shown as an infinite rest time. The bold curves are the smoothed simulation results. The thin curve is the result for a rest time of 2s without smoothing. The symbols indicate the experimental results from the literature[24].

Figure 4 shows the peak value of the viscosity plotted as a function of the rest time, t_r. The viscoelastic relaxation time ($\tau_d = 77\tau_0 = 1.6$ s) and the Rouse time ($\tau_\mathrm{R} = 7.3\tau_0 = 0.15$ s) for the simulation are indicated for comparison. The experimental data are not available for short t_r possibly due to experimental limitations. Consequently, direct comparison can only be made within a limited range of t_r. Nevertheless, the simulation reproduces the experiment reasonably well when $t_r \sim \tau_\mathrm{R}$, where the peak value increases with increasing t_r to reach the same value as under the initial shear. However, for $t_r > \tau_\mathrm{d}$, the viscosity overshoot is insensitive to t_r in the simulation, whereas it increases with t_r in the experiment. This difference is probably due to the MWD, which is neglected in the simulation.

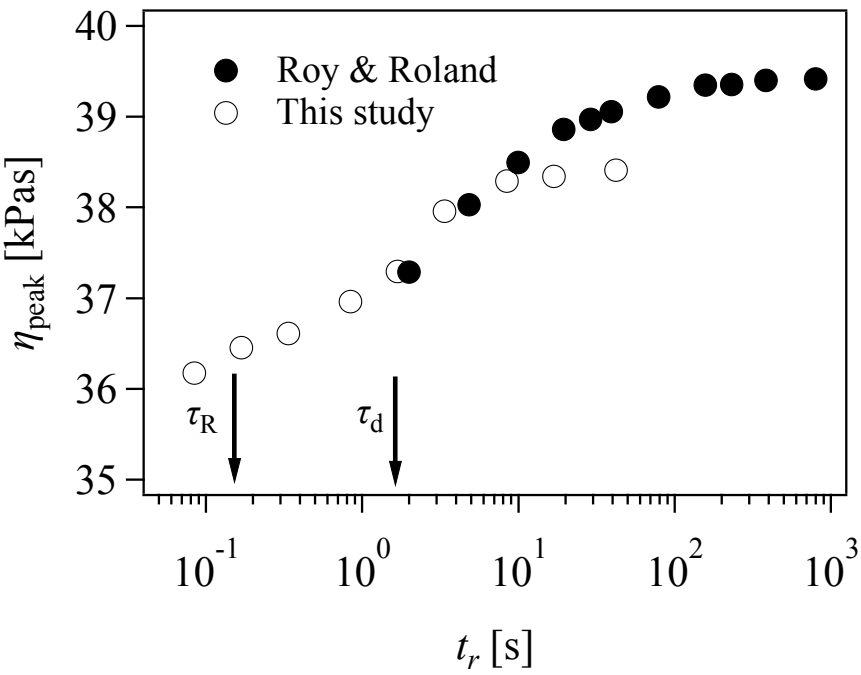

Figure 4 Peak value of the viscocity overshoot under resumed shear as a function of rest time at a shear rate of 1sec^{-1}. The filled and unfilled symbols are the experimental[24] and simulation results, respectively. The viscoelastic relaxation time and the Rouse time for the simulation are indicated for comparison.

Decoupling analysis

We carried out molecular analysis based on the decoupling approximation[13], which is widely used for molecular constitutive equations;

$$\sigma = \frac{3}{V}\sum r_x r_y \approx 3\nu\lambda^2 S \qquad (1)$$

Here, σ is the shear stress, and the sum is taken for all the strands in the simulation box with volume V. $\mathbf{r} \equiv (r_x, r_y, r_z)$ is the strand vector, ν is the strand number density, $\lambda^2 (\equiv \langle \mathbf{r^2} \rangle)$ is the average strand stretch, and $S (\equiv \langle (r_x r_y)/\mathbf{r^2} \rangle)$ is the average strand orientation.

Figure 5 shows the transient behavior of the aforementioned molecular quantities under the resumed shear for various t_r/τ_0 values at shear rates of 10sec^{-1} and 1sec^{-1}. Note that we hereafter discuss the segment number per chain, Z, instead of ν hereafter. As shown in Fig 3, the magnitude of stress overshoot decreases with an increase of t_r. Being consistent with the stress-optical rule, the orientation exhibits a similar behavior. For a shear rate of 10 s^{-1} ($Wi_{\mathrm{d}} = 16$) (Figure 5; left panels), the stretch contributes to the stress to delay the peak position from that of the orientation. The segment number develops similarly to the stretch, but the magnitude of change is much smaller than

that for the stretch. Specifically, λ^2 increased by about 100% (Fig 5, purple line in the second panel from the bottom on the left), whereas the change for Z is less than 20%. The situation is similar for lower strain rates. We note that λ^2 does not start from unity even when the rest time is sufficiently long. Indeed, in our code, λ^2 is slightly (~10%) larger than unity at equilibrium because of the artificial stiffness induced by a numerical cut-off for the monomer number on each strand.

Figure 5 (right panels) shows the case of $\dot{\gamma}$ =1 s^{-1} ($Wi_{\mathrm{d}} = 1.6$), where the stress is dominated by the orientation, and the changes for λ^2 and Z are less pronounced. Consequently, the stress overshoot is dominated by the orientation, and the strand density plays a secondary role. This result is consistent with that of Iannirubeto and Marrucci[17], who qualitatively reproduced the interrupted shear response using a tube model without chain stretch and variable entanglement density.

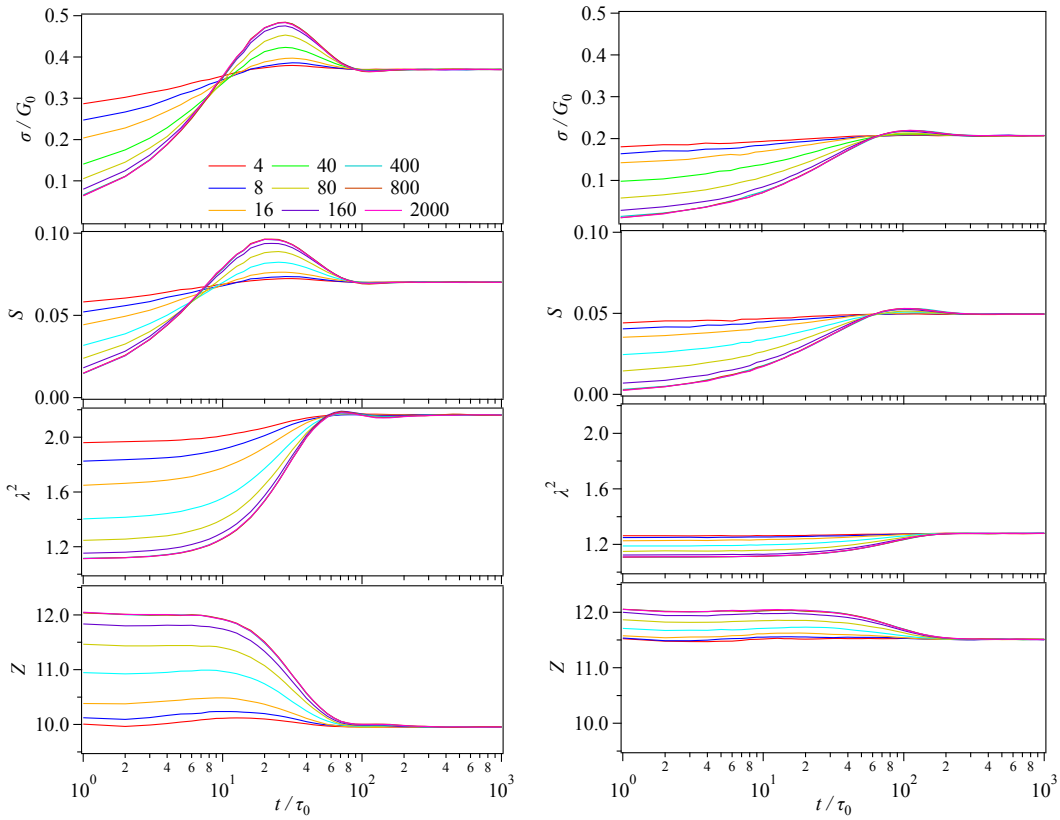

Figure 5 Time development of stress, orientation, stretch, and segment number per chain (from top to bottom) under resumed shear. The shear rates are 10 s^{-1} (left panel) and 1s^{-1} (right panel). The normalized rest time (t_r/τ_0) is indicated in the figure. Note that the curves for rest times longer than 400 ($\gg \tau_{\mathrm{d}}$) overlap.

Structural relaxation during the rest

We now discuss whether the recovery of stress overshoot under resumed shear reflects structural relaxation during the rest after the initial shear. Although the stress overshoot is dominated by the orientation under resumed shear, as seen in Figure 5, the magnitude of overshoot may correlate with the relaxation of other molecular characteristics.

Figure 6 shows the relaxation of stress and molecular characteristics after the initial shear. The orientational relaxation is similar to the stress relaxation, which decays to zero during τ_{d}. The stretch decreases to an equilibrium value reflecting the chain contraction, and the longest relaxation time is comparable to τ_{d} rather than τ_{R}. The number of entanglements per chain recovers from a reduced value, and the recovery time is close to τ_{d}. We note that in the original CCR theory[44,56], the entanglement density is assumed to be constant, whereas the entanglement renewal is accelerated under shear. However, molecular simulations[27,57–59] have revealed that the entanglement density decreases under fast flows as a consequence of CCR.

One may argue that the relaxation time of stretch would be τ_{R} rather than τ_{d}. However, we note that the contraction with τ_{R} is considered for the contour length in the tube theory[30], and not for each segment. Indeed, even for our model, the relaxation time of the contour length is τ_{R}, as reported previously[18]. Meanwhile, for the segment stretch, a retarded contraction has been reported[60,61]. This retardation is due to the reduced number of entanglements as a result of CCR, as mentioned above. When a fast and large deformation results in disentanglements, the number of Kuhn steps on each strand becomes larger than the equilibrium value. In such a configuration, the tension acting on each strand becomes weaker, thereby slowing contraction. Because the entanglement density recovers its equilibrium state via reptation, the relaxation time of segment stretch is close to τ_{d} rather than τ_{R}[60,61].

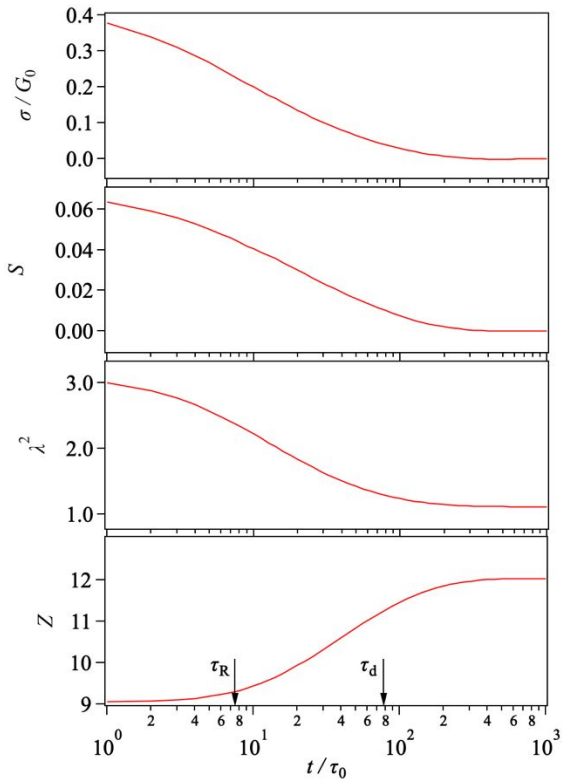

Figure 6 Relaxation from the steady state under a shear rate of 10 s^{-1} for stress, segment orientation, segment stretch, and segment number per chain from top to bottom.

To compare the relaxation behaviors in Figure 6 with each other, we define the relaxation functions as follows:

$$\varphi_\sigma(t) = A_\sigma \sigma(t) \quad (2)$$

$$\varphi_S(t) = A_S S(t) \quad (3)$$

$$\varphi_\lambda(t) = A_\lambda(\lambda^2(t) - 1) \quad (4)$$

$$\varphi_Z(t) = A_Z(1 - Z(t)/Z_0) \quad (5)$$

Figure 7 shows the relaxation functions plotted with the normalized linear relaxation modulus $G(t)/G_0$. The parameters in Eqs 2-5, A_σ, A_S, A_λ and A_Z, were chosen to match the functions with $G(t)/G_0$ for $t \geq \tau_d$; these parameters depend on the shear rate. In this regime, all relaxation functions overlap with $G(t)/G_0$ (broken curve) showing the identical relaxation time of τ_d. In the short-time range ($t < \tau_d$), most of the relaxation functions depend on the shear rate. Because of the non-linearity imposed by the shear, the stress relaxation, $\varphi_\sigma(t)$ (red curve), does not coincide with $G(t)$, and the intensity of the fast relaxation modes increases with an increase of shear rate. Similar behavior is seen for the orientational relaxation, $\varphi_S(t)$ (yellow curve), which overlaps with $\varphi_\sigma(t)$ for low shear rates; this similarity is consistent with the stress-optical rule. Meanwhile, for high shear rates, the orientational relaxation becomes much lower than $\varphi_\sigma(t)$ owing to the contribution

of stretch. The stretch relaxation $\varphi_\lambda(t)$ (green curve) shows a growth of the intensity for fast relaxation modes for fast shear rates due to the chain stretch. $\varphi_Z(t)$ (blue curve) is almost insensitive to the shear rate. Interestingly, only for this relaxation function, fast modes do not appear, even for high shear rates. This behavior can be rationalized if the recovery of Z is dominated by reptation motion as assumed in the tube theory[30]. Furuichi et al.[60] have reported such behavior for PCN simulations under large step shear deformations.

We now compare the relaxation function and the recovery of stress overshoot under resumed shear. From the recovery behavior shown in Figure 4, we define the mitigation function, M_η, for the recovery of viscosity overshoot as a function of t_r as

$$M_\eta(t_r) = B_\eta\left(1 - \eta_{\mathrm{peak}}(t_r)/\eta_{\mathrm{peak}}(\infty)\right) \qquad (6)$$

Here, B_η is a numerical constant that depends on the shear rate. Assuming that t_r and the relaxation period in Figure 5 are compatible, we plot M_η (unfilled circles in Figure 7) with a value of B_η that attains reasonable comparison between M_η and the relaxation functions. Note that the value of M_η is not available for the lowest shear rate, because we did not observe any overshoot for this case. For the other shear rates, M_η is close to φ_Z, and these two functions are almost insensitive to the shear rate, exhibiting no growth of the intensity for fast relaxation modes. To be fair, we note that there is considerable uncertainty for M_η under low shear rates.

One may argue that similar mitigation functions could be defined for the molecular quantities as well. However, such an analysis is not straightforward. For example, as seen in Figure 4, there is no peak for Z. For λ^2, although a faint peak is observed, it is not located at the same position as that for η. As mentioned above, S behaves similarly to η. However, the peak positions do not coincide at high shear rates owing to the contributions of Z and λ^2 to the stress.

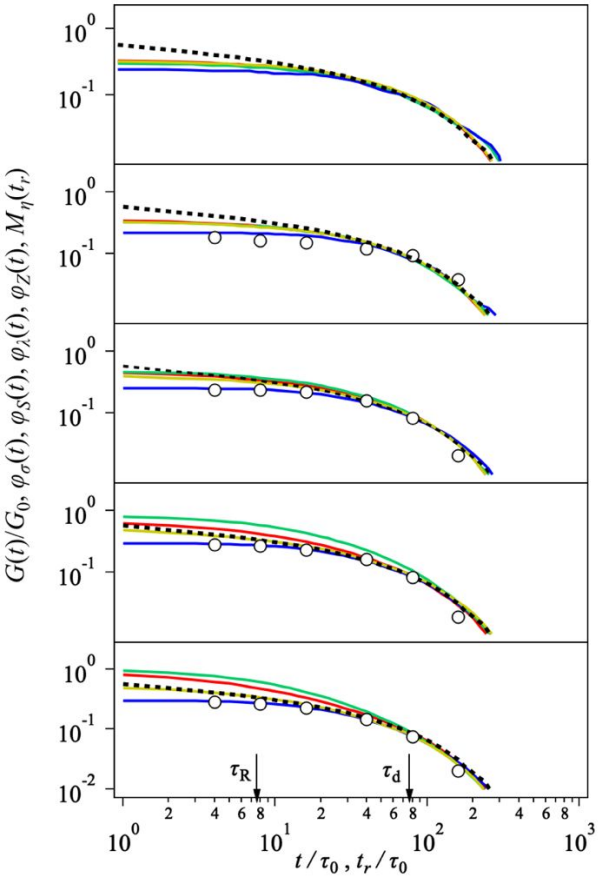

Figure 7 Relaxation functions for stress (red), orientation (yellow), stretch (green), and entanglement density (blue), as defined in Eqs. 2-5. The linear relaxation modulus is shown by the broken curve. The mitigation function for the viscosity overshoot defined by Eq. 6 is marked with open circles. The shear rates are 0.5, 1, 2, 5, and 10 s^{-1} from top to bottom. The Rouse time and the longest relaxation time are indicated by the arrows.

Figure 8 shows the numerical constants A and B in Eqs. 2-6 plotted as functions of the shear rate. A_σ (red) and A_S (yellow) are almost insensitive to the shear rate, whereas A_λ (green) and A_Z (blue) decrease with an increase of the shear rate in a power-law manner, for which the exponent is approximately -1. For the mitigation function, M_η, B_η (black) exhibits a similar decay to A_λ and A_Z. These shear rate dependence of A_λ, A_Z and B_η suggest a linear response for the longest relaxation mode of $\varphi_\lambda(t)$, $\varphi_Z(t)$ and $M_\eta(t_r)$.

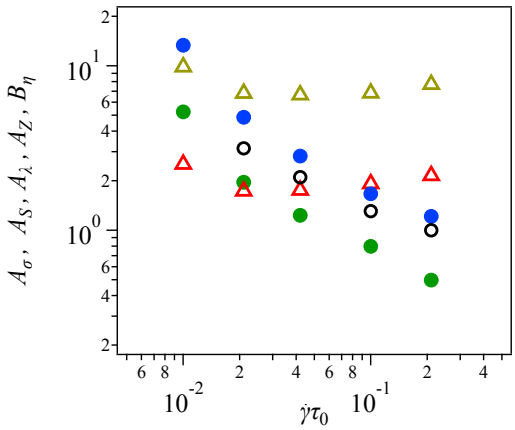

Figure 8 Numerical constants defined for Eqs. 2-6 plotted as functions of the normalized shear rate. A_σ and A_S are represented by unfilled triangles in red and yellow, and A_λ and A_Z are indicated by filled circles in green and blue, respectively. B_η is represented by black unfilled circles.

The similarities between φ_Z and M_η seen in Figures 7 and 8 are unexpected, and we are unable to provide a reasonable explanation for this behavior. We emphasize that the magnitude of the overshoot is not measured for the system during the relaxation. Rather, the overshoot reflects a transient state between a partly relaxed state and a non-equilibrium state under steady shear. Because of this fundamental difference between the relaxation functions and the mitigation function, the results in Figures 7 and 8 cannot be explained by conventional molecular pictures.

We note that the presented results may be related to the model settings and the algorithm used in the conducted simulation, and that other models may give different results. Indeed, because the definition of entanglement is model dependent, the entanglement density and its response to deformations are also model dependent. For example, as mentioned in the Introduction, Ianniruberto and Marrucci[17] argued that the response to interrupted shear can be qualitatively described using a the tube model, whereby the entanglement density is insensitive to deformations. Even among models that assume the entanglement density is reduced under fast and large deformations, the magnitude of entanglement reduction is not universal[59,61]. Meanwhile, we note the network statistics assumed in the PCN model is consistent with the topological network extracted from atomistic molecular simulations[62,63]. In this respect, the presented results would reflect the dynamics of the topological network in some extent.

We also note that some experimental studies suggest flaws in the conventional modeling of entanglement. For exapmle, for the dielectric measurement of polyisoprene under steady shear,

Watanabe et al. [64,65] have reported that the relaxation time and the relaxation intensity measured in the shear gradient direction do not depend on the shear rate. This result means that the end-to-end dimension and its fluctuations along the shear gradient direction do not change, even under fast shear, even when the viscosity shows the shear thinning. To the best of our knowledge, conventional molecular theories cannot reproduce this behavior[25,27]. Teixeira et al. [66] have conducted a direct observation of single DNA molecules under start-up shear. They compared the observed conformational change with that predicted by the tube theory, and found that the observed DNA response is much slower than the theoretical one. PCN simulations failed to reproduce this result as well, even though the viscosity growth was in quantitative agreement[67]. These flaws mean that the conventional molecular theories may not be compatible with the conformational dynamics of polymers, even though they have achieved remarkable success for describing the rheological response of polymers. In this respect, molecular modeling of entanglement is still a challenge, and further improvement is necessary for the conventional models, including PCN. The commonly applied assumptions, such as the homogeneous deformation and the binary contact at the entanglement point, might be problems that should be addressed in future investigations.

CONCLUSIONS

We performed multi-chain slip-link simulations for an entangled polymer under interrupted shear. The simulation reproduced the experimental data for the recovery of viscosity overshoot as a function of rest time. Owing to this agreement, we analyzed the molecular behavior following the decoupling approximation. From the results, we reasonably confirmed that the overshoot is mainly due to segment orientation. To determine if the recovery of the overshoot is related to structural relaxation during the rest after the initial shear, we observed the relaxation of segment orientation, segment stretch, and entanglement density. We compared these relaxation functions with the mitigation of the viscosity overshoot, assuming that the waiting time before the resumed flow is compatible to the relaxation period. The comparison revealed that the mitigation of viscosity overshoot is similar to the relaxation of entanglement density. The similarity between the mitigation of overshoot and the relaxation of entanglement is nontrivial, and might be model-dependent. The effects of the molecular weight distribution would be worth investigating as well. We are currently conducting researches in these directions and the results will be reported elsewhere.

ACKNOWLEDGEMENT

This study is supported in part by Grant-in-Aid for Scientific Research (A) (17H01152) and for Scientific Research on Innovative Areas (18H04483) from JSPS, Ogasawara foundation, and JST-CREST (JPMJCR1992).

REFERENCES

1 J. D. Huppler, I. F. Macdonald, E. Ashare, T. W. Spriggs, R. B. Bird and L. A. Holmes, *Trans. Soc. Rheol.*, 1967, **11**, 181–204.

2 R. A. Stratton and A. F. Butcher, *J. Polym. Sci. Part A-2 Polym. Phys.*, 1973, **11**, 1747–1758.

3 A. V. Tobolsky and R. D. Andrews, *J. Chem. Phys.*, 1945, **13**, 3–27.

4 M. S. Green and a. V. Tobolsky, *J. Chem. Phys.*, 1946, **14**, 80.

5 W. W. Graessley, *J. Chem. Phys.*, 1965, **43**, 2696–2703.

6 M. Doi and S. F. Edwards, *J. Chem. Soc. Faraday Trans. 2*, 1978, **74**, 1802.

7 J. M. Dealy and W. K.-;W. Tsang, *J. Appl. Polym. Sci.*, 1981, **26**, 1149–1158.

8 E. Menezes and W. Graessley, *J. Polym. Sci. Polym. Phys. Ed.*, 1982, **20**, 1817–1833.

9 J. Sanchez-Reyes and L. A. Archer, *J. Rheol. (N. Y. N. Y).*, 2003, **47**, 469–482.

10 C. G. Robertson, S. Warren, D. J. Plazek and C. M. Roland, *Macromolecules*, 2004, **37**, 10018–10022.

11 S. Q. Wang, Y. Wang, S. Cheng, X. Li, X. Zhu and H. Sun, *Macromolecules*, 2013, **46**, 3147–3159.

12 P. G. Santangelo and C. M. Roland, *J. Rheol. (N. Y. N. Y).*, 2001, **45**, 583–594.

13 D. S. Pearson, A. D. Kiss, L. J. Fetters and M. Doi, *J. Rheol. (N. Y. N. Y).*, 1999, **33**, 517–535.

14 Y. Masubuchi and H. Watanabe, *ACS Macro Lett.*, 2014, **3**, 1183–1186.

15 J. Cao and A. E. Likhtman, *ACS Macro Lett.*, 2015, **4**, 1376–1381.

16 Y. Masubuchi and H. Watanabe, *Nihon Reoroji Gakkaishi*, 2016, **44**, 65–68.

17 G. Ianniruberto and G. Marrucci, *ACS Macro Lett.*, 2014, **3**, 552–555.

18 M. Doi and S. F. Edwards, *J. Chem. Soc. Faraday Trans. 2*, 1978, **74**, 1818.

19 R. S. Graham, E. P. Henry and P. D. Olmsted, *Macromolecules*, 2013, **46**, 9849–9854.

20 Y. Masubuchi, J.-I. Takimoto, K. Koyama, G. Ianniruberto, G. Marrucci and F. Greco, *J. Chem. Phys.*, 2001, **115**, 4387–4394.

21 Y. Masubuchi, *Annu. Rev. Chem. Biomol. Eng.*, 2014, **5**, 11–33.

22 Y. Masubuchi, in *Computer Simulation of Polymeric Materials*, Springer Singapore, Singapore, 2016, pp. 101–127.

23 Y. Masubuchi, in *Reference Module in Materials Science and Materials Engineering*, Elsevier, 2016, pp. 1–7.

24 D. Roy and C. M. Roland, *Macromolecules*, 2013, **46**, 9403–9408.

25 Y. Masubuchi, H. Watanabe, G. Ianniruberto, F. Greco and G. Marrucci, *Nihon Reoroji Gakkaishi*, 2004, **32**, 197–202.

26 T. Yaoita, T. Isaki, Y. Masubuchi, H. Watanabe, G. Ianniruberto and G. Marrucci, *Macromolecules*, 2012, **45**, 2773–2782.

27 T. Uneyama, Y. Masubuchi, K. Horio, Y. Matsumiya, H. Watanabe, J. A. Pathak and C. M.

Roland, *J. Polym. Sci. Part B Polym. Phys.*, 2009, **47**, 1039–1057.

28 Y. Masubuchi, G. Ianniruberto and G. Marrucci, *Nihon Reoroji Gakkaishi*, 2018, **46**, 23–28.

29 Y. Masubuchi, G. Ianniruberto and G. Marrucci, *Soft Matter*, 2020, **16**, 1056–1065.

30 M. Doi and S. F. Edwards, *The Theory of Polymer Dynamics*, Clarendon press, Oxford, 1986.

31 D. W. Mead, R. G. Larson and M. Doi, *Macromolecules*, 1998, **31**, 7895–7914.

32 R. S. Graham, A. E. Likhtman, T. C. B. McLeish and S. T. Milner, *J. Rheol. (N. Y. N. Y).*, 2003, **47**, 1171.

33 K. Kremer and G. S. Grest, *J. Chem. Phys.*, 1990, **92**, 5057.

34 C. C. Hua and J. Schieber, *J. Chem. Phys.*, 1998, **109**, 10018–10027.

35 J. D. Schieber, J. Neergaard and S. Gupta, *J. Rheol. (N. Y. N. Y).*, 2003, **47**, 213.

36 M. Doi and J. -i. Takimoto, *Philos. Trans. R. Soc. London Ser. A-Mathematical Phys. Eng. Sci.*, 2003, **361**, 641–650.

37 S. Shanbhag, R. G. Larson, J. Takimoto and M. Doi, *Phys. Rev. Lett.*, 2001, **87**, 195502.

38 A. Baumgartner and K. Binder, *J. Chem. Phys.*, 1981, **75**, 6.

39 J. T. Padding and W. J. Briels, *J. Chem. Phys.*, 2001, **115**, 2846.

40 S. Kumar and R. G. Larson, *J. Chem. Phys.*, 2001, **114**, 6937.

41 J. des Cloizeaux, *Europhys. Lett.*, 1988, **5**, 437–442.

42 W. Graessley, *Adv. Polym. Sci.*, 1982, **47**, 67–117.

43 C. Tsenoglou, *ACS Polym. Prepr.*, 1987, **28**, 185–186.

44 G. Marrucci, *J. Nonnewton. Fluid Mech.*, 1996, **62**, 279–289.

45 G. Marrucci, F. Greco and G. Ianniruberto, *Macromol. Symp.*, 2000, **158**, 57–64.

46 T. Uneyama and Y. Masubuchi, *J. Chem. Phys.*, 2012, **137**, 154902.

47 V. C. Chappa, D. C. Morse, A. Zippelius and M. Müller, *Phys. Rev. Lett.*, 2012, **109**, 148302.

48 A. Ramírez-Hernández, F. A. Detcheverry, B. L. Peters, V. C. Chappa, K. S. Schweizer, M. Müller and J. J. de Pablo, *Macromolecules*, 2013, **46**, 6287–6299.

49 M. Langeloth, Y. Masubuchi, M. C. Böhm and F. Müller-plathe, *J. Chem. Phys.*, 2013, **138**, 104907.

50 Y. Masubuchi and T. Uneyama, *Soft Matter*, 2018, **14**, 5986–5994.

51 Y. Masubuchi, G. Ianniruberto, F. Greco and G. Marrucci, *J. Chem. Phys.*, 2003, **119**, 6925–6930.

52 Y. Masubuchi, G. Ianniruberto, F. Greco and G. Marrucci, *J. Nonnewton. Fluid Mech.*, 2008, **149**, 87–92.

53 K. Furuichi, C. Nonomura, Y. Masubuchi, H. Watanabe, G. Ianniruberto, F. Greco and G. Marrucci, *Rheol. Acta*, 2008, **47**, 591–599.

54 Y. Masubuchi, *Nihon Reoroji Gakkaishi(Journal Soc. Rheol. Japan)*, 2020, **48**, 37–42.

55 A. Savitzky and M. J. E. Golay, *Anal. Chem.*, 1964, **36**, 1627–1639.

56 G. Ianniruberto and G. Marrucci, *J. Nonnewton. Fluid Mech.*, 1996, **65**, 241–246.
57 C. Baig, P. S. Stephanou, G. Tsolou, V. G. Mavrantzas and M. Kröger, *Macromolecules*, 2010, **43**, 8239–8250.
58 Y. Masubuchi, *J. Chem. Phys.*, 2015, **143**, 224905.
59 A. P. Sgouros, G. Megariotis and D. N. Theodorou, *Macromolecules*, 2017, **50**, 4524–4541.
60 K. Furuichi, C. Nonomura, Y. Masubuchi and H. Watanabe, *J. Chem. Phys.*, 2010, **133**, 174902.
61 Y. Masubuchi, *Polymers (Basel).*, 2019, **11**, 370.
62 Y. Masubuchi, T. Uneyama, H. Watanabe, G. Ianniruberto, F. Greco and G. Marrucci, *J. Chem. Phys.*, 2010, **132**, 134902.
63 T. Uneyama and Y. Masubuchi, *J. Chem. Phys.*, 2011, **135**, 184904.
64 H. Watanabe, S. Ishida and Y. Matsumiya, *Macromolecules*, 2002, **35**, 8802–8818.
65 K. Horio, T. Uneyama, Y. Matsumiya, Y. Masubuchi and H. Watanabe, *Macromolecules*, 2014, **47**, 246–255.
66 R. E. Teixeira, A. K. Dambal, D. H. Richter, E. S. G. Shaqfeh and S. Chu, *Macromolecules*, 2007, **40**, 2461–2476.
67 Y. Masubuchi, K. Furuichi, K. Horio, T. Uneyama, H. Watanabe, G. Ianniruberto, F. Greco and G. Marrucci, *J. Chem. Phys.*, 2009, **131**, 114906.

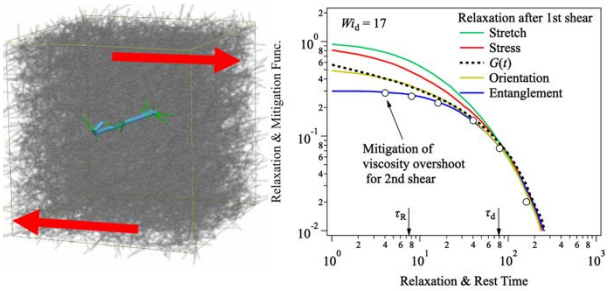

TOC graphic:

In slip-link simulations, recovery of viscosity overshoot in interrupted shear reflects relaxation of entanglement density during interval